










# WASP-186 and WASP-187: two hot Jupiters discovered by SuperWASP and SOPHIE with additional observations by TESS

N. Schanche <sup>1</sup>★, G. Hébrard,<sup>2,3</sup> A. Collier Cameron <sup>1</sup>, S. Dalal,<sup>2</sup> B. Smalley <sup>4</sup>, T. G. Wilson <sup>1</sup>,  
I. Boisse,<sup>5</sup> F. Bouchy,<sup>6</sup> D. J. A. Brown <sup>7,8</sup>, O. Demangeon,<sup>9</sup> C. A. Haswell <sup>10</sup>, C. Hellier,<sup>4</sup> U. C. Kolb,<sup>10</sup>  
T. Lopez <sup>5</sup>, P. F. L. Maxted,<sup>4</sup> D. L. Pollacco,<sup>7,8</sup> R. G. West <sup>7,8</sup> and P. J. Wheatley <sup>7,8</sup>

<sup>1</sup>Centre for Exoplanet Science, SUPA, School of Physics and Astronomy, University of St Andrews, St Andrews KY16 9SS, UK

<sup>2</sup>Institut d'astrophysique de Paris, Université Pierre & Marie Curie, UMR7095 CNRS, 98 bis boulevard Arago, F-75014 Paris, France

<sup>3</sup>Observatoire de Haute-Provence, CNRS, Université d'Aix-Marseille, F-04870 Saint-Michel-l'Observatoire, France

<sup>4</sup>Astrophysics Group, Keele University, Staffordshire ST5 5BG, UK

<sup>5</sup>Laboratoire d'Astrophysique de Marseille, Université de Provence, UMR6110 CNRS, 38 rue F. Joliot Curie, F-13388 Marseille cedex 13, France

<sup>6</sup>Observatoire de Genève, Université de Genève, 51 Chemin des Maillettes, CH-1290 Sauverny, Switzerland

<sup>7</sup>Department of Physics, University of Warwick, Gibbet Hill Road, Coventry CV4 7AL, UK

<sup>8</sup>Centre for Exoplanets and Habitability, University of Warwick, Gibbet Hill Road, Coventry CV4 7AL, UK

<sup>9</sup>Instituto de Astrofísica e Ciências do Espaço, Universidade do Porto, CAUP, Rua das Estrelas, P-4150-762 Porto, Portugal

<sup>10</sup>School of Physical Sciences, The Open University, Milton Keynes MK7 6AA, UK

Accepted 2020 September 9. Received 2020 September 3; in original form 2020 May 7

## ABSTRACT

We present the discovery of two new hot Jupiters identified from the Wide-Angle Search for Planets (WASP) survey, WASP-186b and WASP-187b (TOI-1494.01 and TOI-1493.01). Their planetary nature was established from SOPHIE spectroscopic observations, and additional photometry was obtained from Transiting Exoplanet Survey Satellite. Stellar parameters for the host stars are derived from spectral line, infrared flux method, and isochrone placement analyses. These parameters are combined with the photometric and radial velocity data in a Markov chain Monte Carlo method to determine the planetary properties. WASP-186b is a massive Jupiter ( $4.22 \pm 0.18 M_J$ ,  $1.11 \pm 0.03 R_J$ ) orbiting a mid-F star on a 5.03-d eccentric ( $e = 0.327 \pm 0.008$ ) orbit. WASP-187b is a low-density ( $0.80 \pm 0.09 M_J$ ,  $1.64 \pm 0.05 R_J$ ) planet in a 5.15-d circular orbit around a slightly evolved early F-type star.

**Key words:** planets and satellites: detection – planets and satellites: individual: WASP-186b – planets and satellites: individual: WASP-187b.

## 1 INTRODUCTION

While hot Jupiters are relatively rare, occurring for less than 1 star in 100 (Zhou et al. 2019), they are valuable because they are extreme examples of planetary-system formation. Because these planets have deep transits and short periods, they are well suited for discovery by ground-based surveys such as the Hungarian-made Automated Telescope Network (Bakos et al. 2004), HATSouth (Bakos et al. 2013), the Qatar Exoplanet Survey (Alsubai et al. 2013), the Kilodegree Extremely Little Telescope (Pepper et al. 2007), the Wide-Angle Search for Planets (WASP; Pollacco et al. 2006), and the Next-Generation Transit Survey (Wheatley et al. 2018). As these small-aperture ground surveys are able to detect planets around bright stars, the resulting planet population is useful for follow-up studies of atmospheric composition and structure using occultation and transmission spectroscopy (e.g. Sing et al. 2015; Line et al. 2016).

In this study, we present the discovery of two new hot Jupiter planets: WASP-186b and WASP-187b (TOI-1494.01 and TOI-1493.01). Using radial velocity (RV) data from SOPHIE as well as photometry from WASP and Transiting Exoplanet Survey Satellite (TESS), we determine joint probability distributions for the system parameters. In

Section 2, we describe the observations of both stars with Section 3 describing the method used to fit the planet transit and RV data. Finally, Section 4 provides discussion of the new planets in the context of the known population of exoplanets.

## 2 OBSERVATIONS

Both WASP-186 and WASP-187 were originally flagged as candidates in the WASP survey data after an initial search of the data using the box least-squares method (Kovács, Zucker & Mazeh 2002) using the implementation from Collier Cameron et al. (2006). The planetary nature of both candidates was established with follow-up RV data from the SOPHIE spectrograph (Perruchot et al. 2008; Bouchy et al. 2009b). Additionally, both of these planets were recently observed in photometry taken by the TESS (Ricker et al. 2015). A list of all of the observations can be found in Table 1, with further information found in the following sections.

### 2.1 WASP photometry

WASP-186 was observed by SuperWASP beginning in 2006 and ending in 2014 with a total of 81 014 30-s exposures. The star was originally flagged for further review in 2016 July after inspection of

\* E-mail: ns81@st-andrews.ac.uk

**Table 1.** Summary of available photometric and RV observations for WASP-186 and WASP-187.

Date	Source	No. of observation
<i>WASP-186b</i>		
2006 Aug–2014 Jan	SuperWASP	81 014
2019 Oct–2019 Nov	<i>TESS</i>	821
2016 Nov–2017 Nov	SOPHIE HE	25
<i>WASP-187b</i>		
2004 Jun–2011 Nov	SuperWASP	15 278
2019 Oct–2019 Nov	<i>TESS</i>	821
2014 Dec–2016 Aug	SOPHIE HR	19
2016 Sep–2017 Feb	SOPHIE HE	13

the light curve. WASP-187 was observed from 2004 until 2011 with a total of 15 278 observations. In 2014, the target was flagged for further observations.

The ORCA-TAMTFA transit-search run, which includes multi-season data on 480 fields in the region around the celestial equator that was observed by both SuperWASP and WASP-South, 716 fields from SuperWASP only and 553 from WASP-South only, is the largest and most homogeneous data set available for WASP. As such, the photometry from this run was used as the basis for analysis by the machine learning method described in Schanche et al. (2019). This work combined the results of a random forest classifier and convolutional neural network to find and rank transit candidates. The field in which WASP-186 was identified as a candidate is not part of this run; however, WASP-187 was included and was identified as a good planetary candidate.

## 2.2 SOPHIE spectroscopy

Both WASP-186 and WASP-187 were observed with the SOPHIE spectrograph, first to establish the planetary nature of the SuperWASP transiting candidates, and then to determine their masses and orbital eccentricities. SOPHIE is dedicated to high-precision RV measurements at the 1.93-m telescope of the Haute-Provence Observatory (Perruchot et al. 2008; Bouchy et al. 2009b) and is widely used for SuperWASP follow-up (e.g. Collier Cameron et al. 2007a; Hébrard et al. 2013; Schanche et al. 2019).

WASP-187 was observed between 2014 December and 2016 August in high-resolution (HR) mode with a resolving power  $R = 76\,000$  and fast readout mode. Further data were taken between 2016 September and 2017 February in high-efficiency (HE) mode with a resolving power  $R = 40\,000$  and slow readout mode. HR and HE observations could present a systematic RV shift, so they are considered below as independent data sets. WASP-186 was observed between 2016 November and 2017 November, only in HE mode and slow readout mode. Two low signal-to-noise observations of WASP-186 were not used.

The spectra were extracted using the SOPHIE pipeline (Bouchy et al. 2009b) and the radial velocities were measured from the weighted cross-correlation with a numerical mask (Baranne et al. 1996; Pepe et al. 2002). They were corrected for the CCD charge transfer inefficiency (Bouchy et al. 2009a) and their error bars were computed from the cross-correlation function (CCF) using the method presented by Boisse et al. (2010). Following the method described in Pollacco et al. (2008) and Hébrard et al. (2008), we estimated and corrected for moonlight contamination by using the second SOPHIE fibre aperture that is targeted on the sky while the first aperture points towards the star. The monitoring of constant

**Table 2.** SOPHIE measurements of the planet-host stars.

BJD <sub>UTC</sub>	RV (km s <sup>-1</sup> )	±1σ (km s <sup>-1</sup> )	Bisect. <sup>a</sup> (km s <sup>-1</sup> )	Exp. (s)	SNR <sup>b</sup>
WASP-186 = TOI-1494 (HE mode)					
7719.3870	-5.655	0.031	-0.071	257	25.3
7721.5162	-6.064	0.033	-0.120	420	26.3
7744.3659	-5.628	0.031	-0.082	149	25.9
7745.3613	-6.244	0.031	-0.150	165	25.7
7746.3741	-6.230	0.031	-0.092	208	26.2
7778.2913	-5.529	0.045	-0.076	900	19.6
7791.3104	-6.528	0.043	0.107	1200	23.2
7792.2705	-5.843	0.039	0.067	272	25.3
7977.6056	-6.280	0.025	-0.109	900	36.0
7988.6111	-5.669	0.015	-0.070	900	55.9
7989.6207	-5.511	0.013	-0.092	900	61.1
7992.5287	-6.371	0.032	-0.001	229	26.0
8003.5848	-5.762	0.040	-0.115	412	25.1
8008.6203	-5.724	0.033	-0.086	282	25.3
8036.4419	-5.855	0.035	-0.098	382	26.4
8037.5082	-6.559	0.014	-0.090	900	59.2
8038.4968	-5.910	0.035	-0.034	321	26.6
8039.5341	-5.548	0.031	-0.122	196	26.1
8040.4692	-5.533	0.032	-0.074	263	26.2
8041.4421	-5.816	0.029	-0.044	188	29.0
8052.4838	-6.547	0.031	-0.127	147	25.9
8053.4492	-5.898	0.032	-0.108	342	25.6
8054.4030	-5.556	0.035	-0.086	514	25.2
8057.4893	-6.554	0.038	-0.237	441	25.5
8085.4759	-5.537	0.035	-0.030	245	26.7
WASP-187 = TOI-1493 (HR mode)					
7020.3536	-20.287	0.029	-0.144	1400	37.5
7047.2607	-20.262	0.057	-0.072	1400	16.9
7247.6246	-20.236	0.039	-0.100	508	26.0
7275.6507	-20.188	0.038	-0.121	407	25.7
7303.4805	-20.284	0.020	0.028	1400	45.1
7306.5457	-20.222	0.039	-0.271	708	25.1
7309.5569	-20.217	0.041	-0.061	994	25.0
7331.5082	-20.194	0.023	-0.194	684	39.7
7332.5412	-20.151	0.026	-0.225	628	37.2
7333.5243	-20.258	0.030	-0.051	1400	33.9
7334.4887	-20.241	0.022	-0.195	655	39.4
7335.3682	-20.281	0.036	-0.090	300	25.4
7401.2935	-20.295	0.038	-0.070	676	25.0
7623.5982	-20.224	0.037	-0.053	384	25.1
7624.6495	-20.217	0.045	-0.171	445	22.1
7625.6060	-20.098	0.036	-0.243	499	24.9
7627.6290	-20.228	0.038	-0.157	446	25.3
7628.6165	-20.333	0.038	-0.150	520	25.1
7629.5948	-20.275	0.041	-0.077	1619	23.1
WASP-187 = TOI-1493 (HE mode)					
7658.6570	-20.348	0.026	-0.111	638	32.6
7659.5249	-20.327	0.015	-0.164	916	50.8
7660.4893	-20.276	0.024	-0.113	319	32.0
7661.5282	-20.205	0.024	-0.117	281	32.1
7681.5194	-20.243	0.027	-0.104	445	31.8
7682.5562	-20.188	0.027	-0.168	258	32.6
7720.4122	-20.338	0.024	-0.137	277	32.3
7721.5065	-20.375	0.025	-0.076	545	33.0
7744.3363	-20.198	0.023	-0.158	138	32.2
7745.3565	-20.260	0.023	-0.113	171	32.0
7746.3691	-20.339	0.023	-0.016	181	33.1
7778.2806	-20.335	0.023	-0.163	485	33.0
7792.2768	-20.305	0.029	-0.166	263	30.3

Notes. <sup>a</sup>Bisector spans; error bars are twice those of the RVs.

<sup>b</sup>Signal-to-noise ratio per pixel at 550 nm.

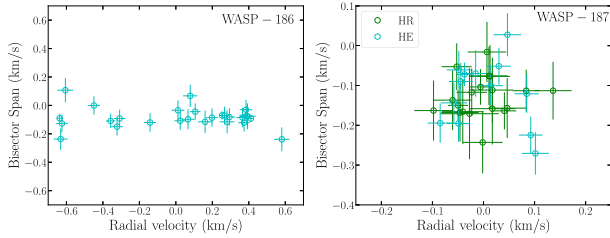


**Figure 1.** Bisector spans as a function of radial velocities for WASP-186 (left) and WASP-187 (right). The radial velocities shown in  $x$ -axis are obtained after subtracting the average RV. For WASP-187, green and blue circles correspond to the data taken in HE and HR modes, respectively. Note that the  $55.4\text{ m s}^{-1}$  fitted shift between HR and HE RVs of WASP-187 is corrected here.

**Table 3.** Initial stellar parameters from the spectroscopic ( $T_{\text{eff}}$ ,  $\log g$ ,  $\text{Fe}/\text{H}$ , and  $v \sin i$ ), isochrone placement ( $M_*$  and age), and *Gaia* + IRFM ( $\varpi$ ,  $R_*$ ) analysis of WASP-186 and WASP-187.

Parameter	WASP-186	WASP-187
$T_{\text{eff}}$ (K)	$6300 \pm 100$	$6100 \pm 100$
$\log g$	$4.1 \pm 0.2$	$3.8 \pm 0.2$
$\text{Fe}/\text{H}$	$-0.08 \pm 0.14$	$0.0 \pm 0.11$
$v \sin i$ ( $\text{km s}^{-1}$ )	$15.6 \pm 0.9$	$15.3 \pm 1.0$
$M_*$	$1.21^{+0.07}_{-0.08}$	$1.53^{+0.07}_{-0.09}$
Age (Gyr)	$3.1^{+1.0}_{-0.8}$	$2.55^{+0.49}_{-0.25}$
Parallax $\varpi$ (mas)	$3.563 \pm 0.042$	$2.667 \pm 0.048$
$R_*$ ( $R_{\odot}$ )	$1.46 \pm 0.02$	$2.87 \pm 0.05$

stars revealed no significant instrumental drifts at the epochs of the observations.

The radial velocities are reported in Table 2. They have larger uncertainties than is typical for SOPHIE due to the rotational line broadening. The resulting CCFs have full width at half-maximum of 22 and 21  $\text{km s}^{-1}$  for WASP-186 and WASP-187, respectively. Still, they show significant variations in phase with the SuperWASP transit ephemeris, with semi-amplitudes corresponding to companions in the planetary-mass regime.

Radial velocities measured using different stellar masks (F0, G2, K0, or K5) produce variations with similar amplitudes, so it is unlikely that these variations are produced by blend scenarios composed of stars of different spectral types. We also checked for signals in the line asymmetry due to blending or magnetic activity using the line bisector measured using the approach of Boisse et al. (2010). They are plotted in Fig. 1 and show no variations correlated with RVs (Pearson correlation coefficients of  $-0.29$  and  $-0.03$  for WASP-186 and WASP-187, respectively). We can thus conclude that the RV variations are not due to spectral-line profile changes attributable to blends or stellar activity, but rather to Doppler shifts due to planetary-mass companions.

### 2.3 TESS photometry

In 2019 October and November, both candidates were observed in Sector 17 of the *TESS* mission and given the designations as *TESS* Objects of Interest (TOI)-1494.01 and TOI-1493.01 with four transits observed for each target. However, a momentum dump at the beginning of the observation run coincided with the first transit of WASP-186 leading the affected transit to appear deeper. We therefore remove the first transit from further analysis. Although the event did not disrupt a transit for WASP-187, we remove the data for this

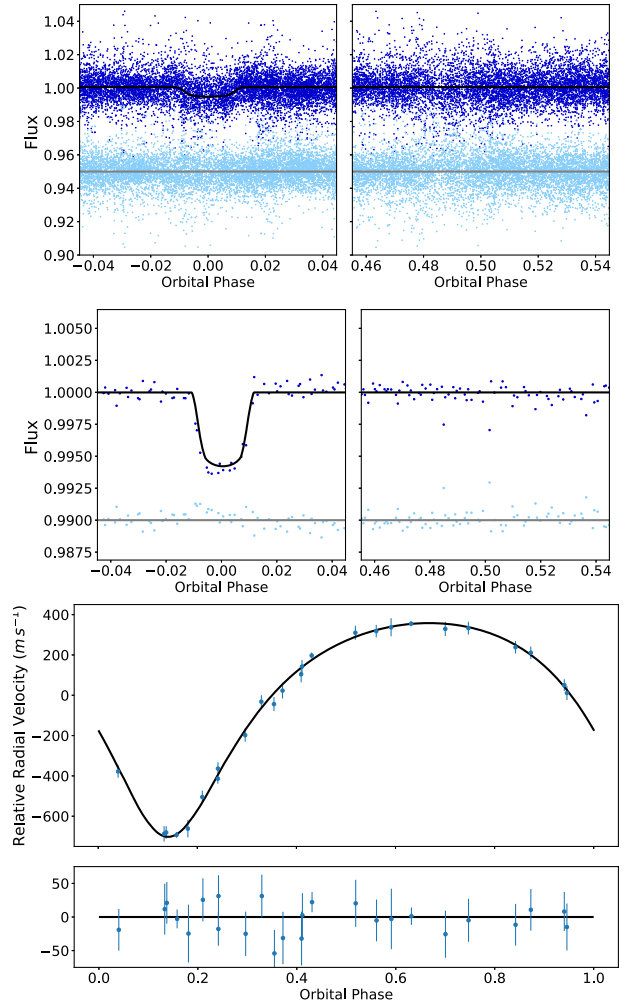


**Figure 2.** WASP (top), *TESS* (middle), and SOPHIE (bottom) data for WASP-186b phase folded on the best-fitting period. Residuals to the fit are shown below the data.

time frame to remove any impact on the out-of-transit measurement. Additionally, the data surrounding spacecraft perigee was removed for both light curves. The full frame images have a cadence of 30 min, with each image comprising a stack of 2-s exposures over that time frame. The data were downloaded and the light curves were extracted and long-term trends were removed using the functions provided in the LIGHTKURVE package (Lightkurve Collaboration 2018). We checked both stars for centroid shifts, but no shifts corresponding to the transits were detected, supporting the conclusion that the transits occur on the target star.

## 3 ANALYSIS

### 3.1 Spectral characterization

For each star, the SOPHIE spectra not polluted by Moonlight were shifted to a common RV and co-added. The spectral analyses were performed using the process outlined in Doyle et al. (2013), i.e. the stellar effective temperature ( $T_{\text{eff}}$ ) was found using the  $\text{H}\alpha$  line; the stellar surface gravity ( $\log g$ ) was determined from the Na D and Mg b lines; the metallicity was estimated from the width of several Fe I lines; and the projected rotational velocity ( $v \sin i$ ) was determined

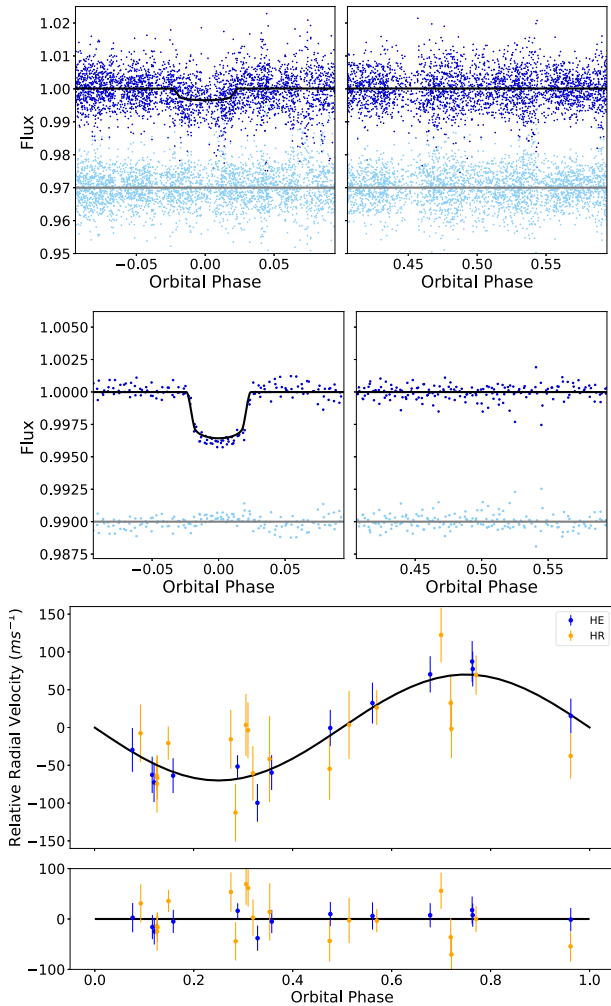


**Figure 3.** WASP (top), *TESS* (middle), and SOPHIE (bottom) data for WASP-187b phase folded on the best-fitting period. Residuals to the fit are shown below the data.

by convolving the SOPHIE spectrum with the instrumental profile and then using spectrum synthesis to fit the Fe I lines, in agreement with results obtained from the CCF using the calibration of Boisse et al. (2010). The results of this spectral analysis can be found in Table 3.

### 3.2 *Gaia* IRFM

The infrared flux method (IRFM), introduced by Blackwell & Shallis (1977), is a semidirect way to measure stellar angular diameter and effective temperature. This method combines flux measurements at different wavelengths with stellar atmospheric models to determine the stellar properties. The IRFM method has been implemented by several groups, e.g. (Alonso, Arribas & Martínez-Roger 1994; Ramírez & Meléndez 2005; González Hernández & Bonifacio 2009; Casagrande et al. 2010). Here, we expand the method with the incorporation of data from *Gaia*.

The magnitudes and corresponding uncertainties for WASP-186 and WASP-187 in the *Gaia* G,  $G_{BP}$  and  $G_{RP}$  bandpasses (Riello et al. 2018) were retrieved from the second data release (DR2) archive (Gaia Collaboration 2018), along with data taken in the *J*, *H*, and *K* filters from the 2MASS survey (Skrutskie et al. 2006) and in the

W1 and W2 (3.4 and 4.6  $\mu\text{m}$ ) bandpasses from the *WISE* survey (Wright et al. 2010). This information is used together with the stellar synthetic spectra atlas of Castelli & Kurucz (2003) to find initial estimates of stellar effective temperature and angular diameter ( $\theta$ ). The *Gaia* parallax measurement ( $\varpi$ ) is then used to produce a radius measurement for the star.

### 3.3 Stellar masses

Using stellar parameters derived from the spectral line fitting (shown in Table 3), stellar masses and ages for WASP-186 and WASP-187 were determined by the isochrone placement functionality of the MCMC tool (Bonfanti & Gillon 2020). Following an Markov chain Monte Carlo (MCMC) approach, with five chains of 100 000 steps and a burn-in fraction of 20 per cent, stellar masses were calculated by interpolating over grids of stellar isochrones and evolutionary tracks to be  $M_* = 1.21^{+0.07}_{-0.08} M_\odot$  and  $M_* = 1.53^{+0.07}_{-0.09} M_\odot$  for WASP-186 and WASP-187, respectively. The corresponding stellar ages were found to be  $3.1^{+1.0}_{-0.8}$  and  $2.55^{+0.49}_{-0.25}$  Gyr. This places WASP-187 near the main-sequence turn-off on evolutionary tracks for the most probable range of masses.

### 3.4 Planetary parameters

The MCMC approach is commonly used in exoplanet model fitting as it is efficiently able to fit a model to the data while at the same time providing a posterior probability distribution of each fitted parameter. The implementation used here is modelled on Collier Cameron et al. (2007b). The code aims to fit the stellar parameters along with the transit and RV data simultaneously.

The jump parameters used to describe the data are chosen to be independent of each other; therefore, the fit of the data to the model relies on the transition of the MCMC jump parameters to the physical variables (For a full description of the transition from these jump parameters to physical variables, see Appendix A). The jump parameters used here are the transit epoch ( $T_c$ ), period ( $P$ ), impact parameter ( $b$ ), transit width ( $w$ ), transit depth  $[(R_p/R_s)^2]$ , received flux ( $f$ ), parallax ( $\varpi$ ), stellar radius ( $R_*$ ), extinction  $[E(B - V)]$ , log of the system error that accounts for zero-point uncertainties in the definitions of the flux-to-magnitude conversions for the different bandpasses in the IRFM calculation ( $\log \sigma_{\text{sys}}$ ), RV amplitude ( $K$ ), RV offset ( $\gamma$ ), and RV jitter ( $\sigma_{\text{jitter}}$ ). For WASP-187 the RV offset and jitter are treated separately for the HR and HE modes. The eccentricity  $e$  and argument of periastron  $\omega$  are parametrized as  $\sqrt{e} \cos \omega$  and  $\sqrt{e} \sin \omega$ ; the fit to the orbit of WASP-187 was, however, found to be consistent with an eccentricity of 0. Therefore, the final MCMC held these values constant. Finally, the transit depth of WASP-187 was underestimated when WASP data were included in the fit. There are no contaminating stars within 114 arcsec. The most likely explanation is a slight dilution of the signal from the detrending of the WASP data. To account for the dilution, we fit an additional positive, constant flux offset to the WASP fluxes for this star, thereby allowing the *TESS* data to dominate the depth determination while retaining the timing information provided by WASP.

Initial fits for the depth, width, impact parameter, period, and epoch for the photometric datasets were done using the Transit Model in the PYCHEOPS v0.6.0 PYTHON package.<sup>1</sup> The power-2 limb darkening coefficients (Macted 2018) are interpolated from tables for *TESS* and WASP separately for the initial fit, as well as at every step in the

<sup>1</sup><https://github.com/pmacted/pycheops>

**Table 4.** System parameters for WASP-186 and WASP-187.

Parameters	Symbol (unit)	WASP-186	WASP-187
<i>Stellar parameters</i>			
WASP ID		1SWASP J011558.85+213700.9	1SWASP J010953.96+254054.0
TESS ID		TOI-1494.01/TIC-411608801	TOI-1493.01/TIC-15692883
<i>Gaia</i> ID		2790691147020786816	306410392895767680
Right ascension	RA (hh:mm:ss)	01:15:58.85	01:09:53.96
Declination	Dec. (dd:mm:ss)	+21:37:00.9	+25:40:54.0
Visual magnitude	Vmag (mag)	10.82	10.30
TESS magnitude	Tmag (mag)	10.30	9.71
<i>Gaia</i> magnitude	Gmag (mag)	10.65	10.13
Stellar mass	$M_*$ ( $M_\odot$ )	$1.22^{+0.07}_{-0.08}$	$1.54 \pm 0.09$
Stellar radius	$R_*$ ( $R_\odot$ )	$1.47 \pm 0.02$	$2.83 \pm 0.05$
Effective temperature	$T_{\text{eff}}$ (K)	$6361^{+105}_{-82}$	$6150^{+92}_{-85}$
Parallax	$\varpi$ (mas)	$3.571^{+0.044}_{-0.042}$	$2.663^{+0.046}_{-0.043}$
Stellar density	$\rho_s$ ( $\rho_\odot$ )	$0.387^{+0.028}_{-0.027}$	$0.068 \pm 0.005$
Surface gravity	log $g$ (cgs)	$4.193^{+0.028}_{-0.029}$	$3.722 \pm 0.029$
Received flux	$f_* 1e^{-9}$ (cgs)	$1.266^{+0.007}_{-0.006}$	$2.055 \pm 0.008$
Extinction	$E(B - V)$ (mag)	$0.03 \pm 0.02$	$0.09 \pm 0.02$
<i>Planet parameters</i>			
Period	$P$ (d)	$5.026799^{+0.00012}_{-0.00014}$	$5.147878^{+0.00005}_{-0.00009}$
Transit epoch	Tc-2450000	$6237.1195 \pm 0.0009$	$5197.3529^{+0.002}_{-0.0022}$
Transit width	$w$ (h)	$2.704^{+0.048}_{-0.051}$	$5.82^{+0.095}_{-0.091}$
Transit depth	$(R_p/R_s)^2$	$0.0061 \pm 0.0003$	$0.0035 \pm 0.0002$
Planet mass	$M_p$ ( $M_{\text{Jup}}$ )	$4.22 \pm 0.18$	$0.8 \pm 0.09$
Planet radius	$R_p$ ( $R_{\text{Jup}}$ )	$1.11 \pm 0.03$	$1.64 \pm 0.05$
Semimajor axis	$a$ (au)	$0.06^{+0.0012}_{-0.0013}$	$0.0653 \pm 0.0013$
Impact parameter	$b$	$0.84^{+0.01}_{-0.02}$	$0.76 \pm 0.02$
Orbital eccentricity	$e$	$0.33 \pm 0.01$	0 (Fixed)
Argument of periastron	$\omega$	$3.02^{+0.05}_{-0.06}$	0 (Fixed)
Planet density	$\rho_p$ ( $\rho_{\text{Jup}}$ )	$2.881^{+0.3}_{-0.279}$	$0.169^{+0.026}_{-0.023}$
Surface gravity	log $g$ (cgs)	$3.93 \pm 0.03$	$2.87^{+0.05}_{-0.06}$
RV semi-amplitude	$K$ ( $\text{m s}^{-1}$ )	$530.29^{+8.43}_{-8.59}$	$70.0^{+6.84}_{-7.75}$
Zero-point uncertainty	log $\sigma_{\text{sys}}$	$-2.19^{+0.41}_{-0.34}$	$-2.16^{+0.32}_{-0.25}$
RV offset	$\gamma$ ( $\text{m s}^{-1}$ )	$-5866.2^{+5.7}_{-5.6}$	$-20275.3^{+6.9}_{-6.8}$ (HE), $-20220.4^{+9.2}_{-9.3}$ (HR)
RV jitter	$\sigma_{\text{jit}}$ ( $\text{m s}^{-1}$ )	$0.8^{+7.1}_{-7.3}$	$3.6^{+4.8}_{-2.8}$ (HE), $17.0^{+12.7}_{-8.7}$ (HR)

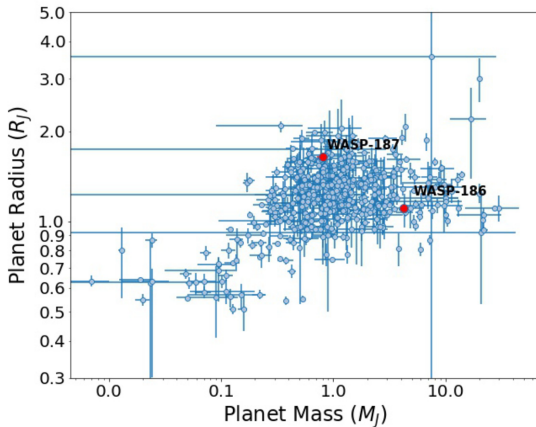


**Figure 4.** Planet mass versus planet radius for all Jupiter-sized planets ( $R_p > 0.5 R_J$ ) with mass and radius measurements. Data for this and subsequent plots was obtained from the NASA Exoplanet Archive <http://exoplanetarchive.ipac.caltech.edu>.

MCMC. The initial fit for the RV parameters were obtained with the RADVEL package.

Several additional pieces of prior information are incorporated into the model. Given  $T_{\text{eff}}$ , log  $g$ , and Fe/H, the stellar surface flux spectrum is computed and attenuated by a galactic extinction law characterized by  $E(B - V)$ . The resulting reddened spectrum is folded through the *Gaia*, 2MASS and *WISE* photon-weighted filter transmission curves and scaled by the zero-points and the squared angular radius to obtain synthetic apparent magnitudes. The residuals of the observed minus synthetic magnitudes in the eight bandpasses and their uncertainties contribute directly to the likelihood at each jump. There is also a prior imposed on the parallax from the measurement in *Gaia* DR2 ( $3.562 \pm 0.043$  and  $2.664 \pm 0.044$  mas for WASP-186 and WASP-187, respectively).  $T_{\text{eff}}$  and log  $g$  priors are imposed from the spectroscopic analysis described in Section 3.1. Finally, the stellar mass prior was determined from the isochrone placement method described in Section 3.3.

The MCMC went through three burn-in phases of 6000, 2000, and 2000 steps, with updates of the jump lengths after each phase. The final MCMC was run for 50 000 steps. The final corner plots for the MCMC runs are shown in Figs B1 through B6 in the appendix.

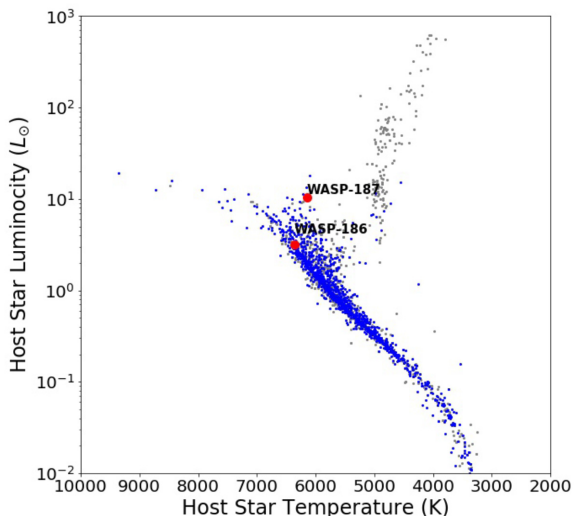


**Figure 5.** HR diagram showing temperature versus stellar luminosity for all stars known to host exoplanets. Stars hosting planets with periods less than 10 d are shown in blue, while stars hosting planets with longer periods are in grey. Note that WASP-187 lies to the right of the main sequence, indicating that the star has entered the post-main-sequence phase of its life.

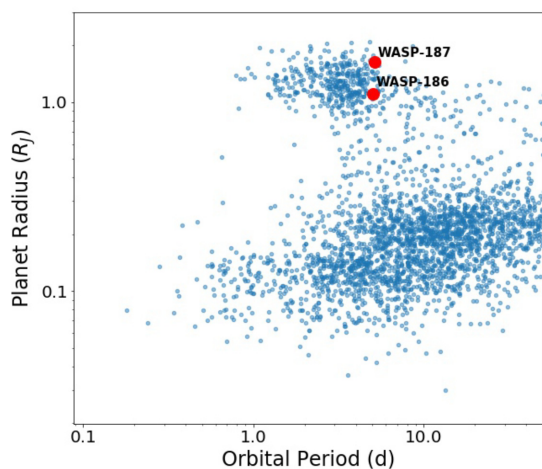


**Figure 6.** Orbital period versus planet radius for all known exoplanets with a period less than 50 d.

The resulting best-fitting model for WASP-186b and WASP-187b are shown in Figs 2 and 3.

#### 4 DISCUSSION AND CONCLUSIONS

The full set of parameters derived for WASP-186b and WASP-187b can be found in Table 4. Note that the values reported for  $T_{\text{eff}}$ , stellar  $\log g$ ,  $\varpi$ ,  $M_*$ , and  $R_*$  were determined by the MCMC analysis and differ slightly from the prior values shown in Table 3.

WASP-186 is a mid-F type star with an effective temperature of  $6361^{+105}_{-82}$  K, agreeing with the spectral determination within errors. The parallax estimate corresponds to a distance of  $280.71^{+13.05}_{-11.96}$  pc (Bailer-Jones et al. 2018). The star is rotating with a  $v \sin i$  of  $15.6 \pm 0.9$  km s $^{-1}$ . As can be seen in Fig. 4, the planet has a radius typical for a hot Jupiter ( $1.11 \pm 0.03 R_{\text{Jup}}$ ), but is quite massive at  $4.22 \pm 0.18 M_{\text{Jup}}$ . WASP-186b therefore fits among the most massive and dense hot Jupiters known. WASP-186b is also notable as the orbit has

an eccentricity of  $0.33 \pm 0.01$ , pointing to late-time high-eccentricity migration, rather than disc migration (Rasio & Ford 1996; Ford & Rasio 2008). Using equation 1 of Dobbs-Dixon, Lin & Mardling (2004) and an estimate for  $Q'_p$  of  $10^6$  in line with the estimation from Yoder & Peale (1981), the time-scale of eccentricity damping via tidal disturbance is of the order of 15.7 Gyr, well above the estimated age of  $3.1^{+1.0}_{-0.8}$  Gyr. WASP-186b therefore joins the small group of massive and eccentric planets, including WASP-150b Cooke et al. (2020), WASP-162b (Hellier et al. 2019), HATS-41b (Bento et al. 2018), XO-3b (Johns-Krull et al. 2008), and HAT-P-2b (Bakos et al. 2007). Finally, the planet has an equilibrium temperature ( $T_{\text{eq}}$ ) of  $1348^{+23}_{-22}$  K, assuming zero albedo and isotropic blackbody re-radiation.

The host star for WASP-187b has begun to evolve away from the main sequence (see Fig. 5), indicated by the stellar effective temperature of  $6150^{+92}_{-85}$  K, mass of  $1.54 \pm 0.09 M_{\odot}$ , and radius of  $2.83 \pm 0.05 R_{\odot}$ . The star is 375.52  $\pm$  0.45 pc away (Bailer-Jones et al. 2018) and has a projected rotation is similar to that of WASP-186 at  $15.3 \pm 1.0$  km s $^{-1}$ , indicating the rotation has slowed since leaving the main sequence (Wolff & Simon 1997). WASP-187b is hotter ( $T_{\text{eq}} = 1726^{+31}_{-29}$ ) and significantly less dense than WASP-186b with a mass of  $0.80 \pm 0.09 M_{\text{Jup}}$  and a radius of  $1.64 \pm 0.05 R_{\text{Jup}}$ , suggesting that this planet could be undergoing re-inflation (Hartman et al. 2016). Both planets have a period of around 5 d, but their radii lie near the low and high radius boundaries for known hot Jupiters of that period (see Fig. 6).

#### ACKNOWLEDGEMENTS

NS acknowledges the support of NPRP grant #X-019-1-006 from the Qatar National Research Fund (a member of Qatar Foundation). ACC acknowledges support from the Science and Technology Facilities Council (STFC) consolidated grant number ST/R000824/1 and United Kingdom Space Agency (UKSA) grant ST/R003203/1. CAH and UCK are supported by STFC under consolidated grant ST/T000295/1. DLP, RGW, and PJW have been supported by STFC consolidated grants ST/P000495/1 and ST/T000406/1. This work was supported by the Swiss National Science Foundation (SNSF). This paper includes data collected by the *TESS* mission. Funding for the *TESS* mission is provided by the NASA Explorer Program. This research made use of Lightkurve, a PYTHON package for *Kepler* and *TESS* data analysis (Lightkurve Collaboration, 2018). This research has made use of the NASA Exoplanet Archive, which is operated by the California Institute of Technology, under contract with the National Aeronautics and Space Administration under the Exoplanet Exploration Program.

#### DATA AVAILABILITY

The data used in this publication can be accessed at <https://doi.org/10.17630/c311756f-557e-4955-b50e-980633ded8f9>.

#### REFERENCES

- Alonso A., Arribas S., Martinez-Roger C., 1994, *A&A*, 282, 684
- Alsubai K. A. et al., 2013, *Acta Astron.*, 63, 465
- Bailer-Jones C. A. L., Rybizki J., Foesneau M., Mantelet G., Andrae R., 2018, *AJ*, 156, 58
- Bakos G. Á., Noyes R. W., Kovács G., Stanek K. Z., Sasselov D. D., Domsa I., 2004, *PASP*, 116, 266
- Bakos G. Á. et al., 2007, *ApJ*, 670, 826
- Bakos G. Á. et al., 2013, *PASP*, 125, 154
- Baranne A. et al., 1996, *A&AS*, 119, 373

- Bento J. et al., 2018, *MNRAS*, 477, 3406  
 Blackwell D. E., Shallis M. J., 1977, *MNRAS*, 180, 177  
 Boisse I. et al., 2010, *A&A*, 523, A88  
 Bonfanti A., Gillon M., 2020, *A&A*, 635, A6  
 Bouchy F., Isambert J., Lovis C., Boisse I., Figueira P., Hébrard G., Pepe F., 2009a, in Kern P., ed., EAS Publ. Ser. Vol. 37, Astrophysics Detector Workshop 2008. p. 247  
 Bouchy F. et al., 2009b, *A&A*, 505, 853  
 Casagrande L., Ramírez I., Meléndez J., Bessell M., Asplund M., 2010, *A&A*, 512, A54  
 Castelli F., Kurucz R. L., 2003, in Piskunov N., Weiss W. W., Gray D. F., eds, Proc. IAU Symp. 210, Modelling of Stellar Atmospheres. Kluwer, Dordrecht, p. A20  
 Collier Cameron A. et al., 2006, *MNRAS*, 373, 799  
 Collier Cameron A. et al., 2007a, *MNRAS*, 375, 951  
 Collier Cameron A. et al., 2007b, *MNRAS*, 380, 1230  
 Cooke B. F. et al., 2020, *AJ*, 159, 255  
 Dobbs-Dixon I., Lin D. N. C., Mardling R. A., 2004, *ApJ*, 610, 464  
 Doyle A. P. et al., 2013, *MNRAS*, 428, 3164  
 Ford E. B., Rasio F. A., 2008, *ApJ*, 686, 621  
 Gaia Collaboration, 2018, *A&A*, 616, A1  
 González Hernández J. I., Bonifacio P., 2009, *A&A*, 497, 497  
 Hartman J. D. et al., 2016, *AJ*, 152, 182  
 Hébrard G. et al., 2008, *A&A*, 488, 763  
 Hébrard G. et al., 2013, *A&A*, 549, A134  
 Hellier C. et al., 2019, *MNRAS*, 482, 1379  
 Johns-Krull C. M. et al., 2008, *ApJ*, 677, 657  
 Kovács G., Zucker S., Mazeh T., 2002, *A&A*, 391, 369  
 Lightkurve Collaboration, 2018, Astrophysics Source Code Library, record ascl:1812.013  
 Line M. R. et al., 2016, *AJ*, 152, 203  
 Maxted P. F. L., 2018, *A&A*, 616, A39  
 Pepe F., Mayor M., Galland F., Naef D., Queloz D., Santos N. C., Udry S., Burnet M., 2002, *A&A*, 388, 632  
 Pepper J. et al., 2007, *PASP*, 119, 923  
 Perruchot S. et al., 2008, Proc. SPIE, 7014, 70140J  
 Pollacco D. L. et al., 2006, *PASP*, 118, 1407  
 Pollacco D. L. et al., 2008, *MNRAS*, 385, 1576  
 Ramírez I., Meléndez J., 2005, *ApJ*, 626, 446  
 Rasio F. A., Ford E. B., 1996, *Science*, 274, 954  
 Ricker G. R. et al., 2015, *J. Astron. Telesc. Instrum. Syst.*, 1, 014003  
 Riello M. et al., 2018, *A&A*, 616, A3  
 Schanche N. et al., 2019, *MNRAS*, 483, 5534  
 Silva Aguirre V. et al., 2015, *MNRAS*, 452, 2127  
 Sing D. K. et al., 2015, *MNRAS*, 446, 2428  
 Skrutskie M. F. et al., 2006, *AJ*, 131, 1163  
 Stassun K. G., Torres G., 2018, *ApJ*, 862, 61  
 Wheatley P. J. et al., 2018, *MNRAS*, 475, 4476  
 Winn J. N., 2009, in Pont F., Sasselov D., Holman M. J., eds, Proc. IAU Symp. 253, Transiting Planets. Cambridge, p. 99  
 Wolff S., Simon T., 1997, *PASP*, 109, 759  
 Wright E. L. et al., 2010, *AJ*, 140, 1868  
 Yoder C. F., Peale S. J., 1981, *Icarus*, 47, 1  
 Zhou G. et al., 2019, *AJ*, 158, 141

## APPENDIX A: STATE TO PHYSICAL VARIABLES

In order to convert the MCMC jump parameters [ $P, w, d, b, \sqrt{e} \cos \omega, \sqrt{e} \sin \omega, f, \varpi, R_*, E(B - V)$ , and  $\log(\sigma_{\text{sys}})$ ] to their physical meaning for the system, the following equations were used.

The eccentricity  $e$  and argument of periastron  $\omega$  are found using

$$e = (\sqrt{e} \cos \omega)^2 + (\sqrt{e} \sin \omega)^2 \quad (\text{A1})$$

and

$$\omega = \tan^{-1}(\sqrt{e} \sin \omega, \sqrt{e} \cos \omega). \quad (\text{A2})$$

The transit duration (in days) that would be expected if the impact parameter were 0 is given by

$$w_0 = \frac{w(1+k)}{\sqrt{(1+k)^2 - b^2}}, \quad (\text{A3})$$

where  $w$  is a proxy for the transit width and  $k$  is the ratio of the planetary to stellar radii,  $R_p/R_*$ . The ratio of the stellar radius to the semimajor axis is then given by

$$\frac{R_*}{a} = \frac{\pi w_0 (1 + e \sin \omega)}{(1+k)P\sqrt{(1-e^2)}}, \quad (\text{A4})$$

where  $P$  is the orbital period in days. As described by Winn (2009),  $\cos i$  and  $\sin i$  are then calculated as

$$\cos i = b \frac{R_*}{a} \frac{1 + e \sin \omega}{(1 - e^2)} \quad \sin i = \sqrt{1 - \cos^2 i}. \quad (\text{A5})$$

The next step is to get the angular radius of the star. First, the radius and parallax of the star are used to get the angular radius ( $\theta \equiv \frac{R_*}{d}$ ):

$$\theta = \frac{R_* (\varpi + 0.082)}{1000 \star 180 \star 3600}, \quad (\text{A6})$$

where  $\varpi$  is the parallax in milli-arcseconds, and the correction of Stassun & Torres (2018) is applied to the parallax.

The orbital separation can then be found by

$$\frac{a}{a_{\oplus}} = \frac{\theta}{\varpi} \frac{a}{R_*}, \quad (\text{A7})$$

with  $a_{\oplus}$  being one astronomical unit and  $\varpi$  expressed in radians.

The mass of the star can then be calculated using Kelper's third law and appropriate unit conversions:

$$\frac{M_*}{M_{\odot}} = \left(\frac{a}{a_{\oplus}}\right)^3 \left(\frac{P}{1 \text{ yr}}\right)^{-2}. \quad (\text{A8})$$

The angular radius is also utilized to find the stellar surface flux  $F$ :

$$F = f/\theta^2. \quad (\text{A9})$$

The stellar surface flux is corrected for extinction iteratively:

$$F_{\text{ext}} = F 10^{0.4 E(B-V) R_{\text{bol}}}. \quad (\text{A10})$$

$R_{\text{bol}}$  used here is the bolometric extinction to reddening ratio, determined by optimizing the fit to stellar radii in the asteroseismic samples provided in Silva Aguirre et al. (2015):

$$R_{\text{bol}} = 2.31 + 0.000509(T_{\text{eff}} - 5894). \quad (\text{A11})$$

The flux is then used to find the effective temperature  $T_{\text{eff}}$ . In this way, the  $T_{\text{eff}}$  and  $E(B - V)$  values are decoupled from the stellar radius.

With the mass and radius of the star now known, we can calculate  $\log g$ .

Finally, the power-2 limb darkening parameters are interpolated from a grid specific to each instrument using the  $\log g$  and  $T_{\text{eff}}$  calculated.

The final physical variables therefore are  $\sin i, \frac{R_*}{a}, k, T_{\text{eff}}, \log g, \theta, M_*, \sigma_{\text{sys}}, e$ , and  $\omega$ .

## APPENDIX B: MCMC RESULTS

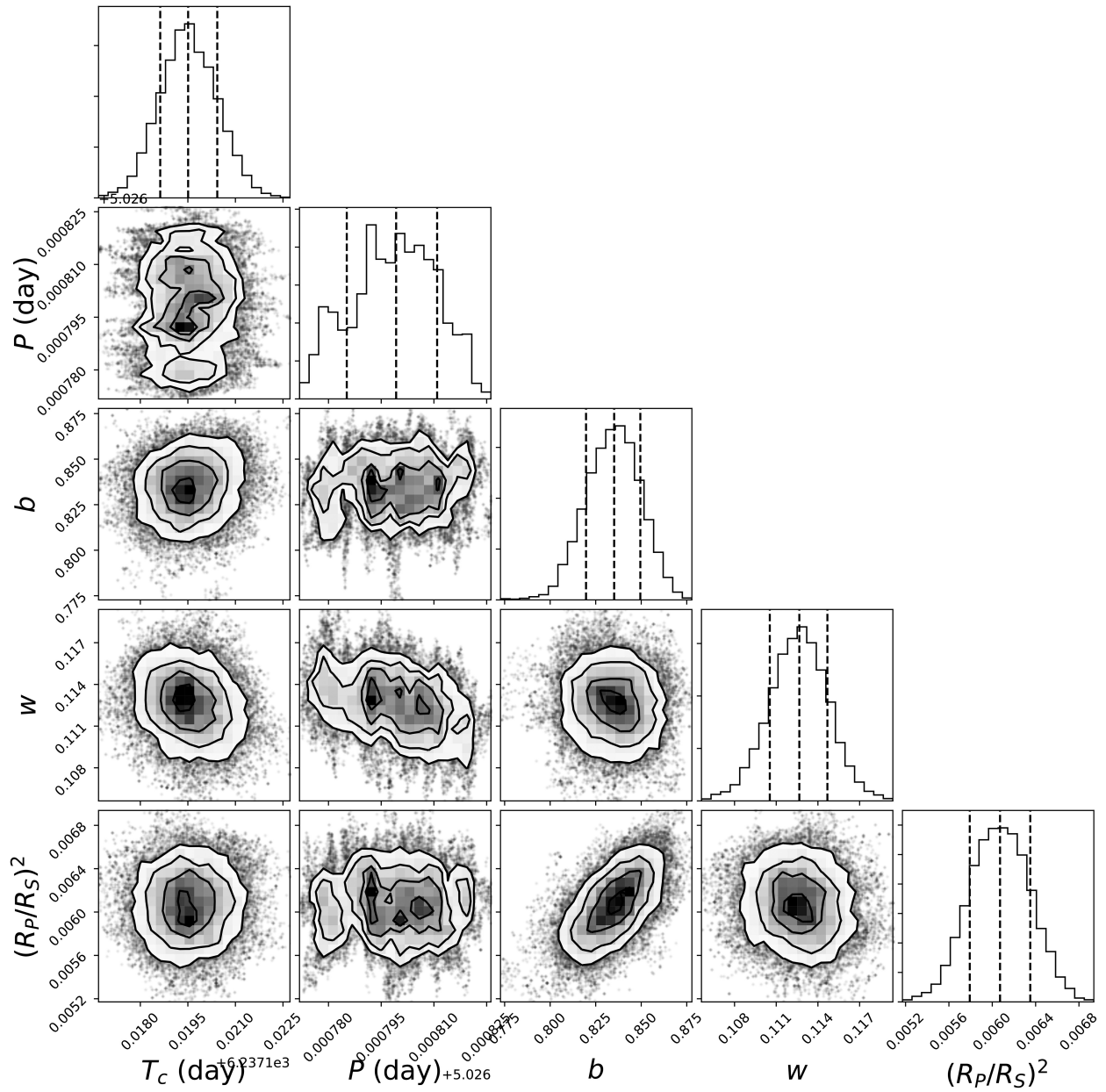


**Figure B1.** Cornerplot of the jump parameters describing the photometric data from the final MCMC run for WASP-186.



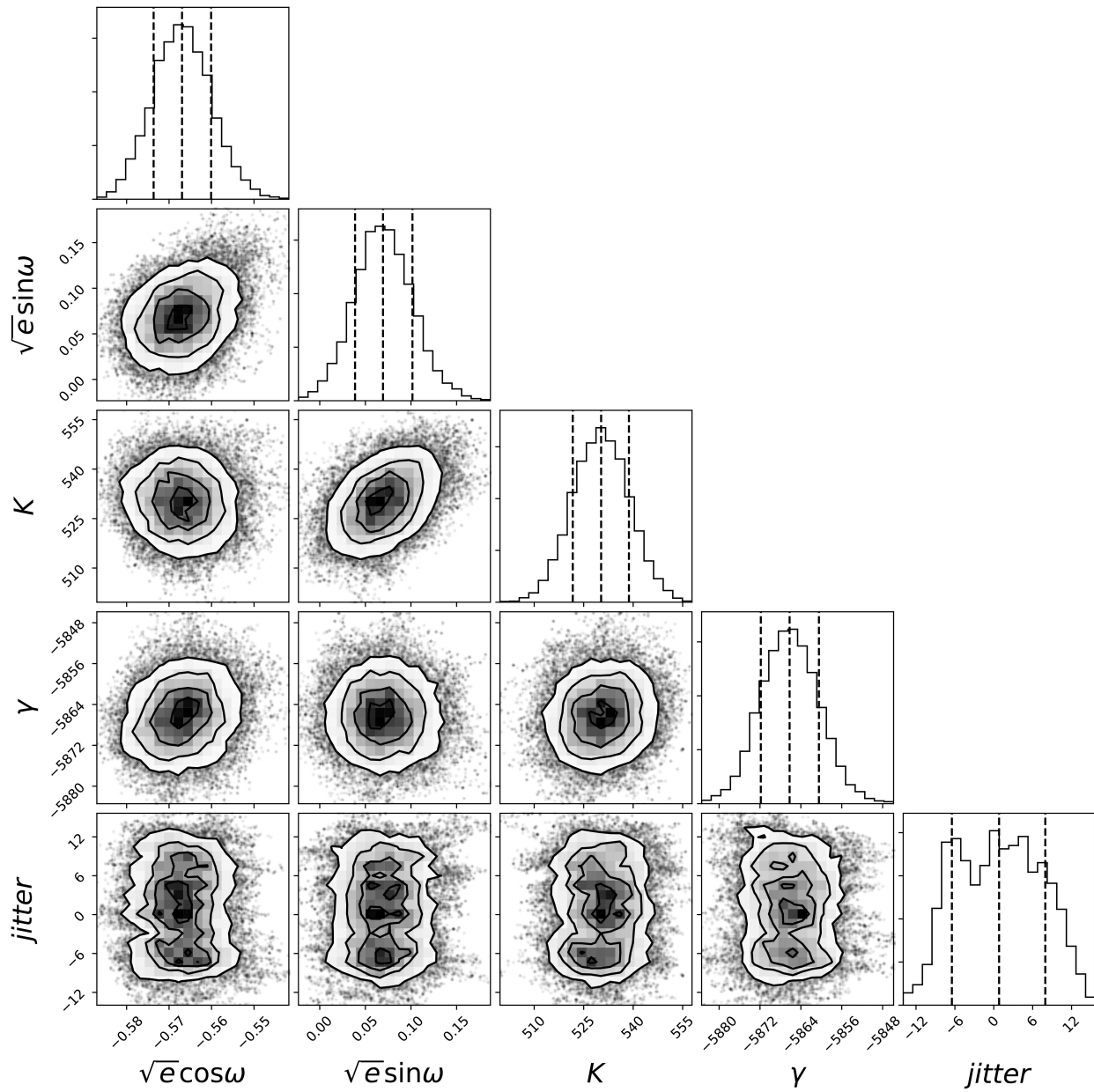


**Figure B2.** Cornerplot of the jump parameters describing the RV data from the final MCMC run for WASP-186.

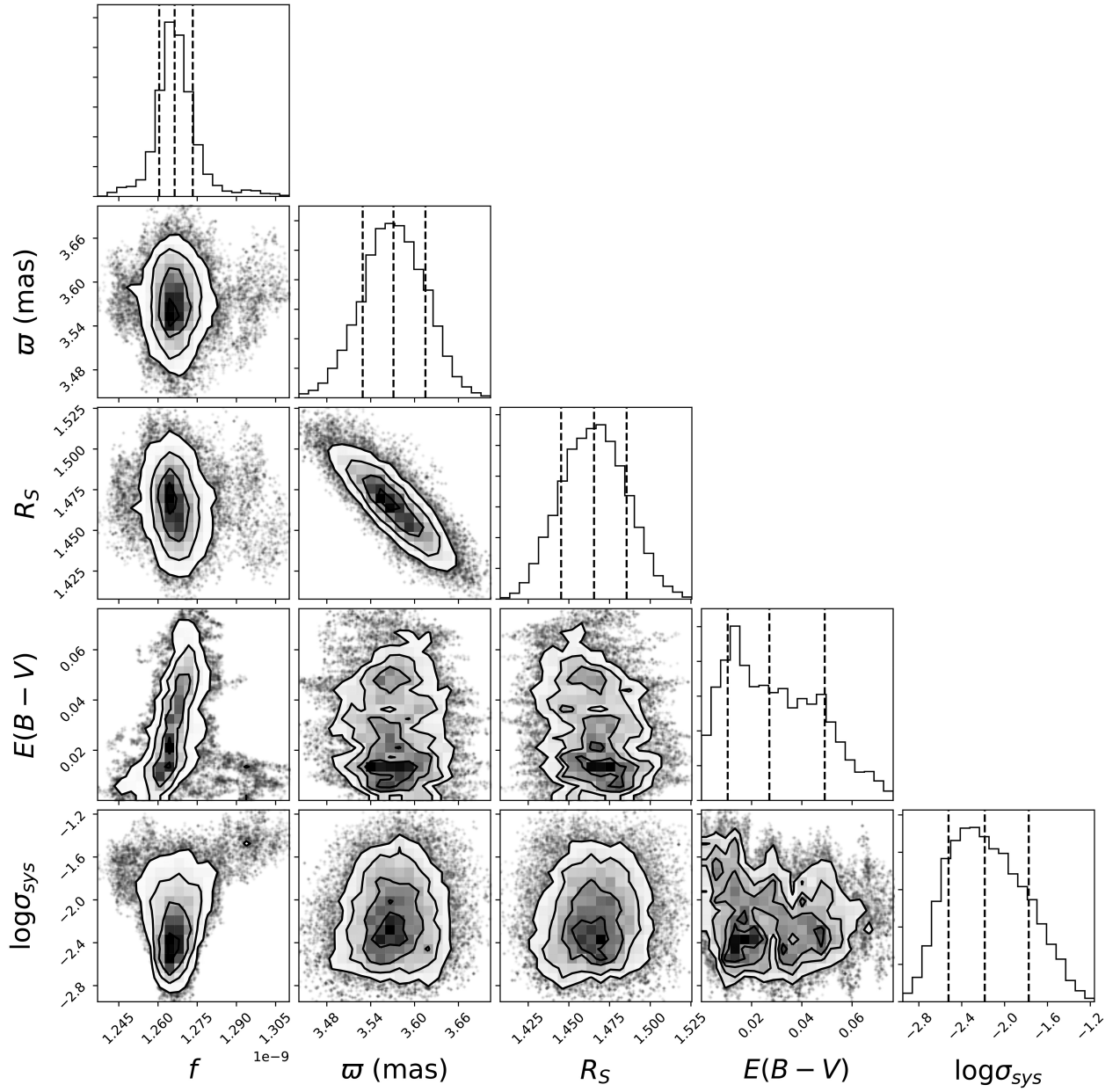
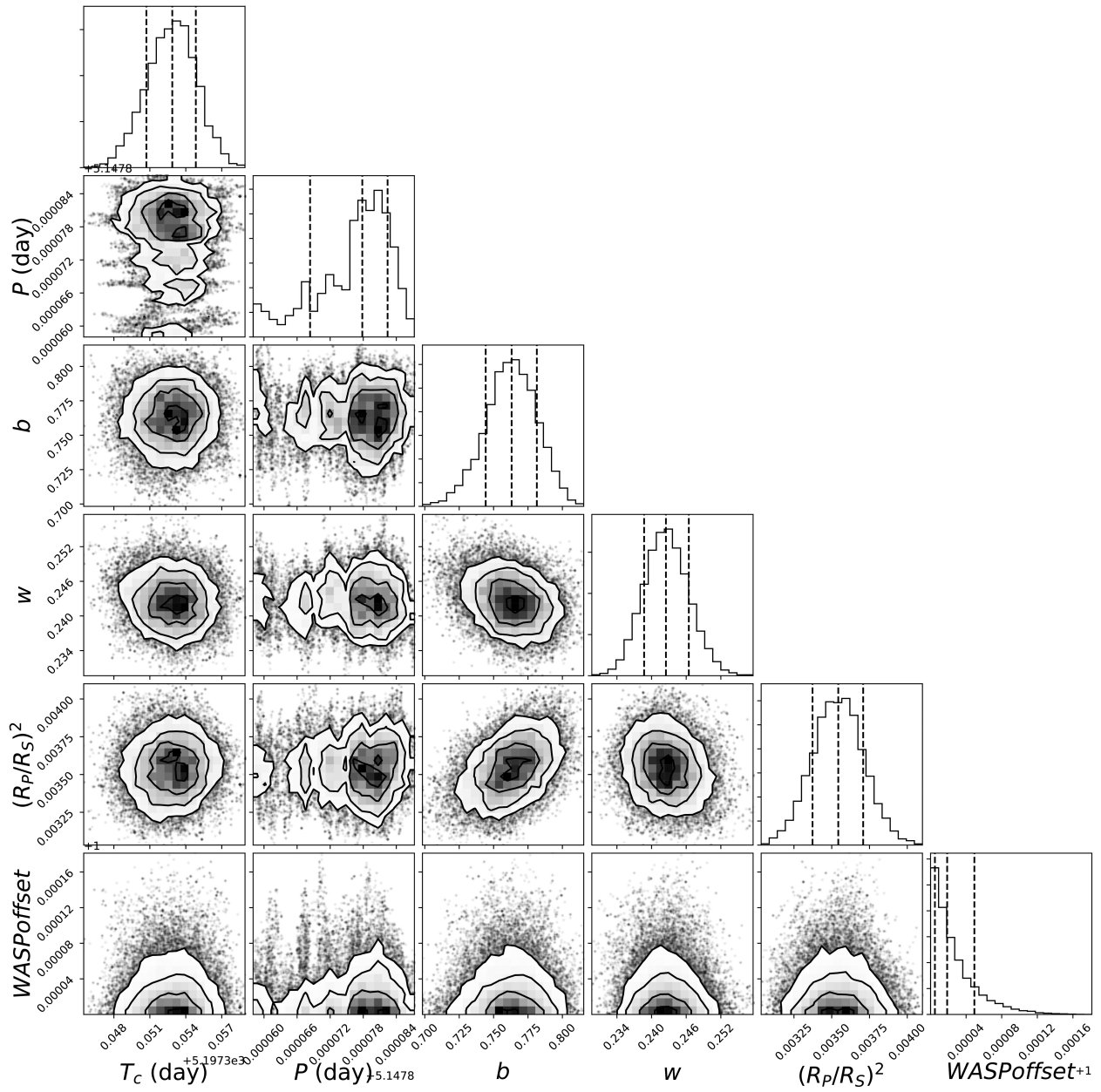


Figure B3. Cornerplot of the jump parameters describing the stellar features from the final MCMC run for WASP-186.



**Figure B4.** Same as Fig. B1 but for WASP-187.

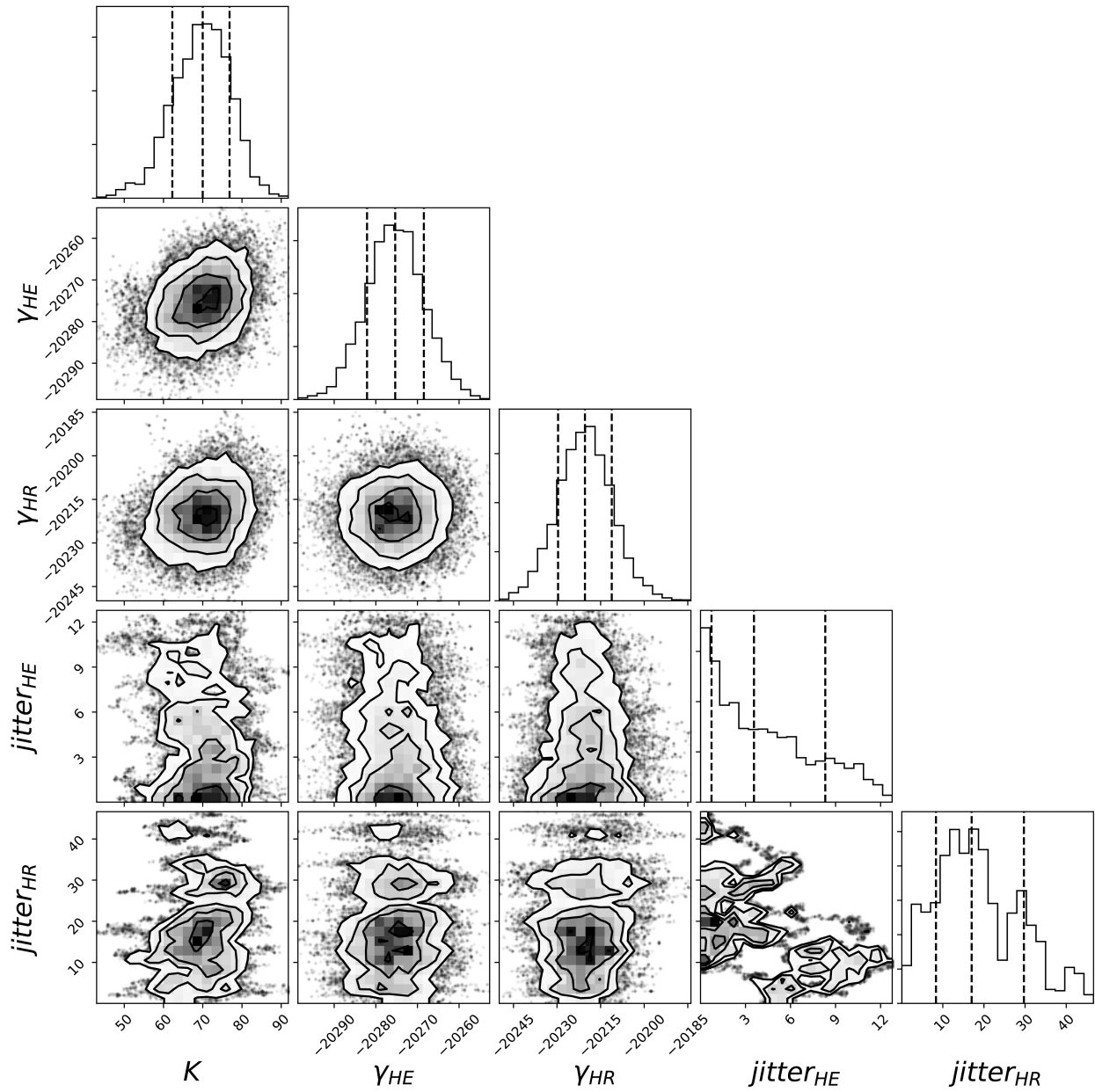
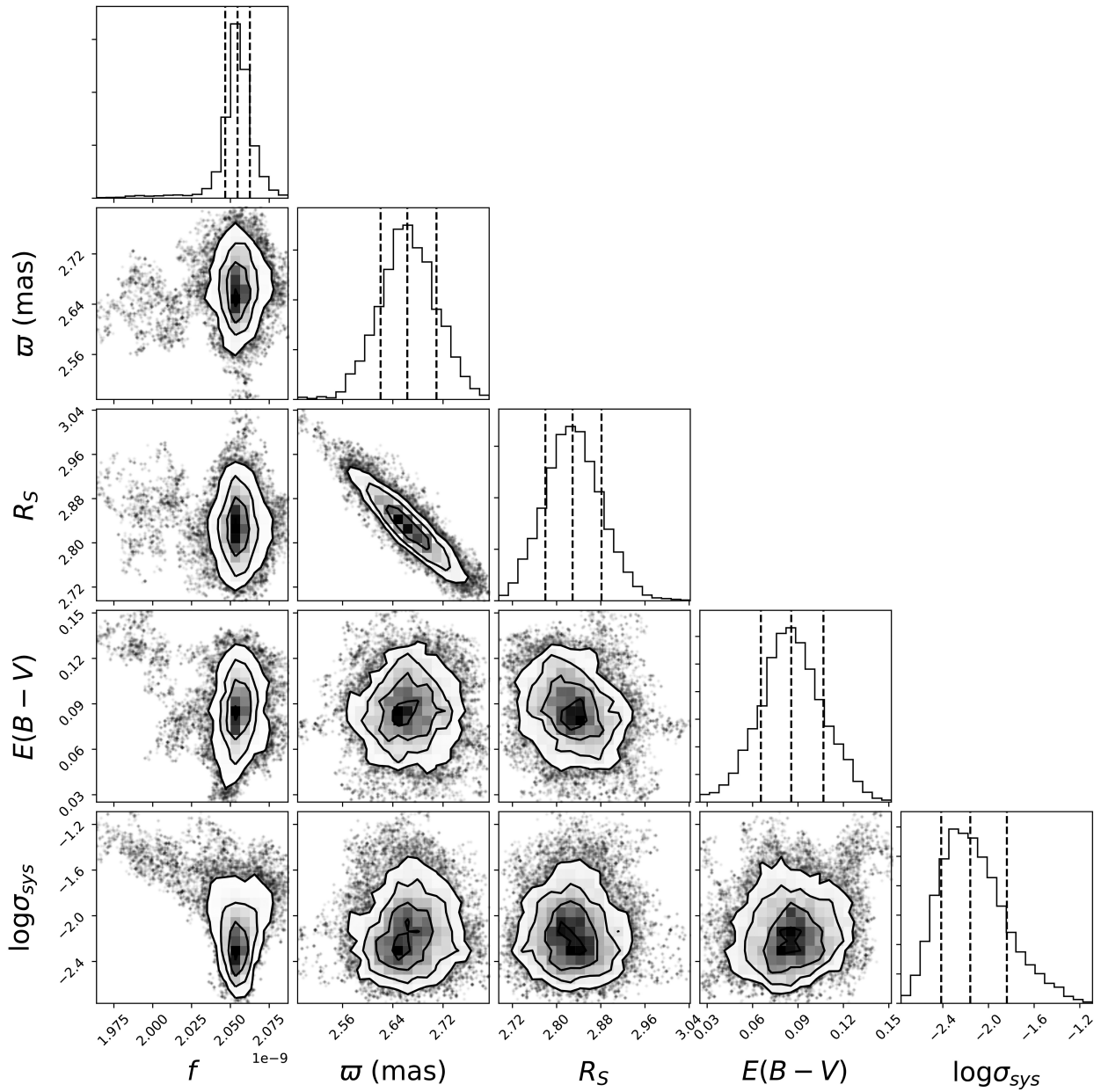


Figure B5. Same as Fig. B2 but for WASP-187.



**Figure B6.** Same as Fig. B3 but for WASP-187.

This paper has been typeset from a  $\text{\TeX}/\text{\LaTeX}$  file prepared by the author.